Article:
Evans, H., Andrews, R., Abedi, F.A. et al. (8 more authors) (2024) Evidence for peri-lacunar remodeling and altered osteocyte lacuno-canalicular network in mouse models of myeloma-induced bone disease. JBMR Plus, 8 (9). ziae093. ISSN 2473-4039

https://doi.org/10.1093/jbmrpl/ziae093

Evidence for peri-lacunar remodeling and altered osteocyte lacuno-canalicular network in mouse models of myeloma-induced bone disease

Holly Evans[1*], Rebecca Andrews[1,2*], Fatma Ali Abedi[1], Alexandria Sprules[1], Jacob Trend[3], Goran Lovric[4], Alanna Green[1], Andrew Chantry[1,2], Claire Clarkin[3], Janet Brown[1,2] and Michelle Lawson[1]

*joint first authors

Affiliations

[1]Division of Clinical Medicine and Mellanby Centre for Musculoskeletal Research, School of Medicine and Population Health, Faculty of Health, University of Sheffield, Sheffield, S10 2RX, UK.

[2]Sheffield Teaching Hospitals, Royal Hallamshire Hospital NHS Foundation Trust, Sheffield, S10 2JF, UK.

[3]School of Biological Sciences, University of Southampton, Southampton, SO17 1BJ, UK.

[4]Swiss Light Source, Paul Scherrer Institut, Forschungsstrasse 111, 5232 Villigen-PSI, Switzerland.

Corresponding author: Dr Michelle Lawson, Division of Clinical Medicine, School of Medicine and Population Health, University of Sheffield, Beech Hill Road, Sheffield, S10 2RX. m.a.lawson@sheffield.ac.uk

Abstract

Myeloma bone disease (MBD) affects approximately 90% of multiple myeloma patients but current treatment options are suboptimal. Therefore, to successfully develop new therapies or optimize current ones, we must improve our fundamental knowledge of how myeloma affects bone microstructure and function. Here we have investigated the osteocyte lacuno-canalicular network (LCN) in MBD, as bone porosity affects bone quality and resilience. We used the syngeneic 5TGM1-C57BL-Kalwrij and the xenograft U266-NSG models at end stage and compared them to healthy controls (naïve). Micro-computed tomography (μCT) and histomorphometry indicated the 5TGM1 and U266 models developed mild and extensive MBD respectively, with the U266 model producing large osteolytic lesions. High-resolution synchrotron micro-CT (SR-μCT) revealed significant osteocyte lacunae changes in U266 bones but not 5TGM1, with a reduction in lacunae number and sphericity, and an increase in lacunae volume compared to naïve. Canalicular length, visualized using histological Ploton silver staining, appeared significantly shorter in 5TGM1 and U266 bones compared to naïve. Canalicular area as a proportion of the bone was also decreased by 24.2% in the U266 model. We observed significant upregulation of genes implicated in peri-lacunar remodeling (PLR), but immunohistochemistry confirmed that the osteocyte-specific protein sclerostin, a known driver of PLR, was unchanged between MBD and naïve bones. In summary, we have demonstrated evidence of PLR and altered organization of the osteocyte LCN in MBD mouse models. The next step would be to further understand the drivers and implications of PLR in MBD, and whether treatments to manipulate PLR and the LCN may improve patient outcomes.

Lay summary

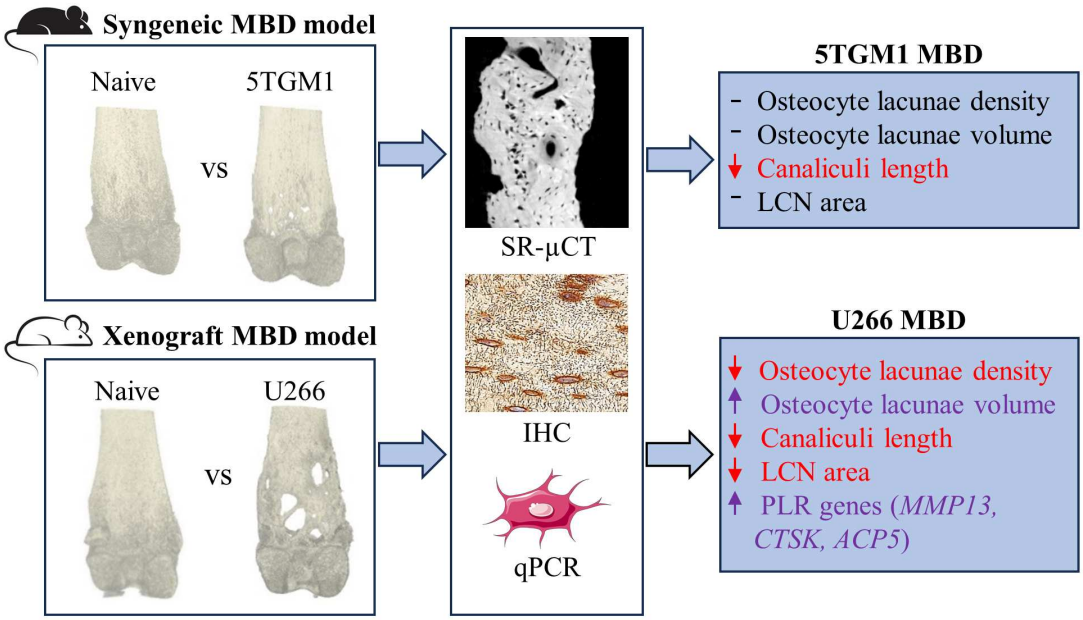
Syngeneic MBD model
Naive
5TGM1
vs
Xenograft MBD model
Naive
U266
vs
SR-µCT
IHC
qPCR
5TGM1 MBD
- Osteocyte lacunae density
- Osteocyte lacunae volume
↓ Canaliculi length
- LCN area
U266 MBD
↓ Osteocyte lacunae density
↑ Osteocyte lacunae volume
↓ Canaliculi length
↓ LCN area
↑ PLR genes (MMP13, CTSK, ACP5)

Multiple myeloma is a blood cancer that causes bone damage in approximately 90% of patients. Currently treatment options for myeloma bone disease (MBD) are suboptimal, leaving patients with chronic pain and increased fracture risk. Therefore, it is important that we improve our fundamental knowledge of how myeloma causes bone damage. With the development of more powerful imaging technologies, this allows us to visualize bone at the sub-micron level. Here we assessed bones from two murine models of MBD (termed 5TGM1 and U266) and compared them to bones from healthy control mice (naïve). Using high resolution imaging (SR-μCT) we found structural changes in the pores where the most abundant bone cells (osteocytes) reside, and that the orientation of their signaling network (lacuno-canalicular network, LCN) is altered in MBD compared to healthy bones. We also found differences in gene expression of key molecules in osteocytes from bones with MBD compared to healthy bones and identified a potential mechanism leading to these changes. The next step would be to use this knowledge to determine how myeloma treatments can affect the osteocyte LCN, as this may allow informed treatment decisions to be made, potentially reducing fracture risk and improving outcomes for patients with MBD.

Key words

Myeloma, osteocytes, bone, lacuno-canalicular network, synchrotron, peri-lacunar remodeling

Introduction

Multiple myeloma is a blood cancer that develops in plasma cells in the bone marrow. Patients often present with myeloma bone disease (MBD) caused by the uncoupling of bone remodeling, resulting in osteolytic lesions and trabecular thinning.[1] Current therapies, such as bisphosphonates and denosumab (receptor activator of nuclear factor kappa-β ligand (RANKL)

inhibitor), target osteoclasts but often leave patients with high fracture risk, possibly due to enhancement and propagation of micro-cracks over time.[2] Therefore, to successfully develop new therapies or optimize current ones, we must improve our fundamental knowledge of how myeloma affects bone. Most research to date has focused on osteoblasts and osteoclasts, with limited knowledge about osteocytes. Therefore, further research into the role of osteocytes and their lacuno-canalicular network (LCN) in MBD is needed, both to fully understand their part in MBD-induced bone fragility, and to further explore whether osteocytes could be targeted therapeutically to treat MBD.

Osteocytes, comprising >90% of the total bone cell population,[3] are derived from terminally differentiated cells of the osteoblast lineage. They reside in lacunae embedded within the mineralized bone matrix and form a dense, intricate dendritic network that allows them to communicate with each other and other bone cells via the LCN.[4] Osteocytes are key regulators of bone remodeling, coordinating osteoblast and osteoclast proliferation and differentiation through signaling pathways.[5, 6] They produce sclerostin, a protein encoded by the *Sost* gene that binds to LRP5/6 receptors and inhibits the Wnt pathway, leading to reduced bone formation. Osteocytes also directly control bone homeostasis through a process called peri-lacunar remodeling (PLR), whereby they resorb and replace the extracellular matrix, comprising type I collagen, that directly surrounds them.[7, 8] PLR has been demonstrated in several mouse lactation studies,[9, 10] but can occur in both male and female mice.[11] Moreover, it is initiated in conditions such as osteomalacia[12] and rickets.[13] Interestingly, sclerostin and TGFβ are known drivers of PLR,[8, 14] both of which are known to be regulatory factors in myeloma.

Studies have shown that patients with MBD have proportionally fewer viable osteocytes than healthy controls.[15] In preclinical MBD models, Ziouti *et al.*[16] have observed enlarged osteocyte lacunae and disorganization in the osteocyte LCN but these changes were not quantified. There is mixed data regarding sclerostin expression in MBD. Giuliani *et al*.[15] found that sclerostin expression by osteocytes in myeloma patients was not significantly different than that in healthy patients; in contrast, Terpos *et al*.[17] reported that patients with symptomatic myeloma had elevated circulating sclerostin compared to healthy patients or those with monoclonal gammopathy of undetermined significance. These differences in sclerostin may be explained by Delgado-Calle *et al*. who observed that myeloma cells increase osteocyte apoptosis, both *in vitro* and *in vivo,* and that myeloma cells upregulate *Sost* (sclerostin gene) mRNA levels in osteocytes *in vitro*.[18] Contrastingly, McDonald *et al*. found minimal difference in *Sost* expression in osteocytes from MBD mice at disease end stage, and no difference in the number of sclerostin-positive osteocytes.[19] Sclerostin expression may, therefore, be dependent on the stage of MBD, limiting efficacy of anti-sclerostin therapies in some patients. However, in preclinical models of MBD, sclerostin inhibition has shown great promise,[19] but as yet therapies such as romosozumab have not been used clinically in myeloma patients, only in osteoporosis.[20, 21]

Osteocytes play a clear role in bone homeostasis, yet much is unknown about how the osteocyte LCN is implicated in MBD pathogenesis. Here, we hypothesized that MBD leads to increased osteocyte apoptosis, resulting in a reduced and disorganized LCN that we can correlate to sclerostin expression. To test this we used two mouse models, one with mild MBD (5TGM1) and one with extensive MBD (U266), and then compared their bones to those from healthy control (naïve, non-tumor controls) mice. Using Ploton silver staining and high-resolution synchrotron micro-CT (SR-μCT), we determined that osteocyte canaliculi appeared shorter in both models, and in the highly osteolytic U266 bones there were fewer osteocyte lacunae.

However, these remaining lacunae were enlarged and the LCN appeared to have an altered organization with reduced area coverage. Isolation of osteocyte-enriched RNA from marrow-flushed U266 whole bones showed key PLR-related genes were upregulated, implying that PLR may be driving the changes seen in the osteocyte lacunae and the LCN.

Material and Methods

Ethical approval

All animal experiments were approved by the University of Sheffield Animal Ethics Committee and the UK Home Office (PPL PP3267943) in strict compliance with the Animal (Scientific Procedures) Act 1986.

Cell lines

5TGM1-GFP and U266-GFP-Luc cells were maintained in RPMI 1640 medium with 10% fetal bovine serum and 50 units/ml penicillin/100μg/ml streptomycin in an atmosphere of 5% CO_2 at 37°C. Cells were confirmed as negative for mycoplasma in the week preceding inoculation.

In vivo studies

5TGM1 model (syngeneic): 6-8 week-old male C57BL/KaLwRijHsd (BKAL) mice (Charles River Laboratories, UK) were injected intravenously (i.v.) with $2x10^6$ 5TGM1-eGFP cells (5TGM1 tumor group, n=8) or PBS (BKAL, naïve control group, n=5). All mice were sacrificed at 3 weeks post-tumor cell injection.

U266 model (xenograft): 9-10 week-old female NOD *scid* gamma (NOD.Cg-*Prkdc*^{scid}*Il2rg*^{tm1Wjl}*/SzJ,* NSG) mice were injected i.v. with 10^6 U266-GFP-luc cells (U266 tumor group, n=8) or PBS (NSG, naïve control group, n=8). All mice were sacrificed at 10 weeks post-tumor cell injection. The U266 model and naïve mice (n=8 or 3/group, respectively) were also used for quantitative real-time PCR (qPCR) of primary osteocytes.

All mice were randomized by weight and group-housed in individual cages with a 12-hour light/dark cycle and had free access to food and water. Experimental mouse group numbers were calculated using power calculations based on previously published data.[22] All analyses were performed blinded.

*Micro-computed tomography (*μCT) and *high-resolution synchrotron micro-CT imaging (SR-*μ*CT)*

Femora and tibiae were fixed in 10% formalin for 48 hours and then stored in 70% ethanol. For *ex vivo* μCT, right femora were scanned on a Skyscan 1272 (Bruker, Switzerland) at 50kV and 200μA at 4.3μm pixel resolution for a 180° scan with 0.7° rotation. A 1mm region of interest 0.4μm from the growth plate was determined, and trabecular bone as a percentage of bone volume (BV/TV), trabecular thickness (Tb. Th) trabecular number (Tb. N), trabecular separation (Tb. Sp), cortical volume (Ct. V) and cortical thickness (Ct. Th) were assessed in this region.as previously described.[23] Bone lesion area as a proportion of total bone surface area (%) was assessed using Osteolytica software as previously detailed.[24]

Swiss Light Source (TOMCAT beamline, Paul Scherrer Institut, Switzerland, Proposal ID 20220399): Right 5TGM1 tibiae at the tibiofibular joint [25, 26] and right U266 femora at the metaphysis were scanned using SR-μCT in absorption and inline phase-contrast imaging mode with 0.65μm pixel size to visualize both bone and osteocytes within lacunae.[27, 28] For each scan, 3000 projection images were captured over a 360° rotation with a fixed energy of 21keV and an exposure time of 120ms, at a sample-to-detector propagation distance of 40mm.

Diamond Light Source (I13-2 beamline, Didcot, UK, Proposal MG31801): Right 5TGM1 femora were scanned at the metaphysis using SR-μCT with 1.625μm pixel size. For each scan, 2000 projections were captured over a 360° rotation with a beam energy of 20keV, a ring current of 300mA and an exposure time of 130ms.

SR-μCT image processing and analysis

SR-μCT datasets were processed, analyzed and imaged using the software Dragonfly (v. 2022 for Windows, Object Research Systems (ORS) Inc, Montreal, Canada).

To analyze the osteocyte lacunae, a region of interest (ROI) was selected for both the femoral metaphysis and the tibiofibular joint. For the femoral metaphysis, this was a 0.5mm section (769 slices) 0.1mm distally from the last visible remaining portion of the growth plate. For the tibiofibular joint, this was a 0.5mm section (769 slices) 0.1mm distally from where the fibula connected to the tibia. Femoral ROIs also went through the additional step of having their trabecular bone removed from the dataset, leaving only the cortex.

For both femoral metaphysis and tibiofibular joint ROI datasets, firstly the cortex was segmented from the background by global thresholding so that a binary image remained, where cortex was white and background was black. A sweep was also performed so that only the largest object remained, removing any unwanted artefacts. Next, a mask of the bone was created, with all pores (not open to the outside) filled in. This was to serve as the base, so that when the original, porous, bone was subtracted from it only the lacunae would remain. Pores were then filtered by volume as reported by Hemmatian *et al*.[29] with those of a volume less than 2000μm³ classed as osteocyte lacunae. Those with a volume greater than 2000μm³ were classed as intracortical canals and excluded. Pores with a volume less than 25μm³ were assumed to be noise and were similarly excluded. Osteocyte lacunae were quantified for the following parameters: density (number per mm³ of cortical bone), proportion (% of cortical bone), mean volume (μm³) and sphericity (relative index, with 1 equaling a perfect sphere).

Histomorphometry and immunohistochemistry

187 Left tibiae were decalcified, wax embedded, then 3μm sections cut and stained for tartrate-
188 resistant acid phosphatase (TRAP) and hematoxylin as previously described.[30] Quantification
189 of tumor burden, osteoclasts and osteoblasts were assessed as previously described.[31]

190 For staining of the osteocyte lacuno-canalicular network, 3μm paraffin-embedded sections
191 were dewaxed and exposed to Ploton silver staining.[32] Sections were stained with 50% silver
192 nitrate solution, and silver staining then developed in a 5% sodium thiosulphate solution.
193 Sections were also counterstained with hematoxylin for visualization of osteocyte nuclei.

194 The LCN was analyzed using Osteomeasure (Osteometrics, Decatur, GA, USA), Fiji (v. 1.543t,
195 National Institutes of Health, USA)[33] and Dragonfly. For quantification of LCN coverage a
196 3-field 1.5mm region, 1.5mm from the growth plate, was assessed and microscope field images
197 taken every 0.5mm. Fiji was used to assess LCN area as a proportion of total bone area.
198 Microscope field images were loaded and for each a ROI encapsulating the entirety of the bone
199 area was drawn and any osteocytes and cement lines removed, so that only bone area and LCN
200 remained. The image was then binarized with the LCN becoming white and the bone surface
201 becoming black. LCN area as a proportion of total bone area was then calculated for each of
202 the 3 fields, before the mean was calculated. For quantification of osteocyte canalicular length,
203 canaliculi arising from each osteocyte lacuna and extending as a single, unbranched projection
204 were traced using Osteomeasure. The mean length was determined by loading microscope field
205 images and measuring all canaliculi from 3 osteocytes per field for a total of 9 osteocytes,
206 before an average canaliculi length was calculated, as previously carried out by Dole *et al*.[8]
207 For 2-D analysis of LCN orientation, microscope field images were loaded into Dragonfly and
208 aligned so that osteocyte lacunae lay as straight to the horizontal plane as possible, with
209 canaliculi thus perpendicular to them in the vertical plane. The image was segmented, so that
210 the LCN became white and the surrounding bone became black. 2D orientation analysis was
211 then performed, with the angle of major axis of each canaliculus measured from the vertical in

degrees. Proportion of canaliculi falling between -20 degrees to 20 degrees around the vertical out of all canaliculi was then assessed.

For sclerostin assessment, decalcified 3µm paraffin-embedded tibial sections were dewaxed and treated with pepsin for antigen retrieval and 3% H_2O_2 for blocking of endogenous peroxidase activity, followed by 10% casein for non-specific protein block. Sections were incubated with primary sclerostin antibody (1:500, R&D, AF1589) followed by incubation with a secondary biotinylated antibody (horse anti-goat IgG biotin, Vector BA – 100, 1:200). Sections were then treated with an avidin-conjugated peroxidase (VectaStain Elite ABC-HROP Kit, Vector Laboratories) and DAB (Vector, ImmPACT DAB, SK-4105). Sclerostin protein was stained in brown and sections were counterstained with hematoxylin. Slides were scanned on a NanoZoomer XR slide scanner (Hamamatsu, Shizuoka, Japan) at 40x, and sclerostin coverage and number of sclerostin-positive osteocytes[34] was quantified using QuPath (v. 0.4.3). A 1.5mm region, 250µm from the growth plate, was assessed.

Quantitative real-time PCR (qPCR)

Prior to sacrifice, presence of tumor and MBD were confirmed in U266 mice as previously described.[22] Right femora (after removal of soft tissue, distal and proximal ends, and marrow) were snap frozen in liquid nitrogen and then homogenized (Precellys Evolution, Bertin Instruments, France) in tri reagent (guanidinium thiocyanate).[8] RNA was extracted using phenol-chloroform and quantified using a Nanodrop spectrophotometer. cDNA was synthesized using a High-Capacity RNA-to-cDNA kit (ThermoFisher Scientific) and qPCR was performed on a QuantStudio 7 with Design and Analysis 2.6.0 software (Applied Biosystems, CA, USA) with TaqMan primers used for quantification of *Dmp1 (dentin matrix acidic phosphoprotein 1)*, *Sost*, *MMP13 (matrix metalloproteinase-13)*, *Ctsk (cathepsin K)*,

Acp5 (acid phosphatase 5, TRAP) and *MMP2 (matrix metalloproteinase-2)* genes relative to *Gapdh*.[36]

Statistical analysis

All data are presented as mean ±SD. Statistical analysis was performed using GraphPad Prism 9 (GraphPad Software, Inc., La Jolla, CA, USA) using unpaired two-tailed Student's t test.

Results

Mice with 5TGM1 or U266 tumors exhibit myeloma bone disease

To first verify that the 5TGM1 and U266 models (Fig 1A-B) successfully resulted in MBD we assessed the bones for the presence of tumor cells, as well as changes in osteoblasts and osteoclasts (Fig 1C-M). Tumor burden was high in both 5TGM1 and U266 (Fig 1C-F, K), and both myeloma models exhibited decreased osteoblast surface coverage and osteoblast number (Fig 1G-J, L, Supplemental Fig 1A). Osteoclast surface coverage and number remained unchanged in the 5TGM1 model but rose significantly in the U266-bearing mice (Fig 1G-J, M, Supplemental Figure 1B). Both myeloma models developed osteolytic lesions in the proximal femur, although these were far more extensive (5-fold higher) in the U266 model (Fig 1N-Q, T). Neither model exhibited lesions in the tibiofibular joint region (Fig 1R-S). For cortical bone, 5TGM1-bearing mice showed no significant change in either cortical volume or cortical thickness compared to naïve, whereas U266-bearing mice exhibited a decreased cortical volume whilst cortical thickness remained unchanged when compared to naïve (Fig 1U-V). For trabecular bone architecture, 5TGM1-bearing mice showed no significant change in trabecular bone volume, but U266-bearing mice exhibited a lower trabecular bone volume (Fig 1W) than naïve controls. Trabecular thickness, trabecular number and trabecular separation were unchanged between disease and naïve in both models (Supplemental Fig 1C-E).

Osteocyte lacunae are enlarged and more ellipsoidal in U266 mice

To determine whether the presence of MBD induced changes in osteocyte lacunae, we examined the femoral metaphysis and tibiofibular joint by high-resolution SR-μCT scanning (Supplemental Fig 1F-J). At the femoral metaphysis, osteocyte lacunar density was unaffected in 5TGM1 mice compared to naïve, but in U266 mice it was significantly decreased (Fig 2A). Lacunar volume as a proportion of total bone volume was similarly unaffected in 5TGM1 compared to naïve, but significantly increased in U266 (Fig 2B). This increase in proportion was driven by a significant doubling in average lacunar volume for U266 compared to naïve, while average lacunar volume remained unchanged for 5TGM1 (Fig 2C, E-H). Lacunar sphericity was also significantly altered in the U266 model with less spherical lacunae compared to naïve, whilst there was no change in sphericity in 5TGM1 (Fig 2D). We also examined the tibiofibular joint region in the 5TGM1 model compared to naïve (Fig 1R-S, Supplementary Fig 1G); this region typically does not develop MBD, and we wanted to test whether the changes in osteocytes found at the femoral metaphysis were systemic or localized. No changes in osteocyte lacunar density, proportion, volume or sphericity were observed in this region (Supplemental Fig 1K-P).

To confirm the enlarged lacunae in U266 bones still housed osteocytes and were not simply empty pits, the lacunae were examined in SR-μCT scans taken using phase-contrasting techniques, which allows the visualization of both high-contrast objects (bone) and low-contrast objects (osteocytes). Solid structures were clearly identifiable within the lacunae, which we believe to be osteocytes. (Fig 2I-L).

5TGM1 and U266 mice have osteocyte canaliculi of a shorter appearance compared to naïve mice

Osteocytes function as part of a complex dendritic network that allows them to communicate with each other. We assessed if MBD altered the coverage and structure of the LCN. We treated

tibial sections with Ploton silver staining and examined a region at the tibial metaphysis. Average apparent canaliculi length was significantly shorter in both 5TGM1 (30.4%) and U266 (29.1%) tibiae compared to naïve tibiae (Fig 3A, C-F). LCN area as a proportion of the bone was also 24.2% lower in U266 tibiae compared to naïve, whilst 5TGM1 tibiae were unaffected (Fig 3B, C-F). To determine whether LCN orientation was altered, the number of canaliculi lying perpendicular to the osteocytes was measured as a proportion of all canaliculi (Fig 3G). U266 tibiae exhibited fewer perpendicular canaliculi compared to naïve, indicating altered LCN organization, whilst 5TGM1 LCN organization was unaffected (Fig 3H-L).

Osteocytes from U266 femora have elevated expression of peri-lacunar remodeling genes

Osteocytes are known to contribute to bone homeostasis by PLR, a process whereby bone surrounding osteocytes is resorbed and deposited. Therefore, we investigated whether the increased lacunar size was associated with PLR. We isolated primary femoral osteocytes from the U266 and naïve (NSG) mice and performed qPCR (Fig 4A-C) for a panel of genes: *Dmp1* and *Sost*, which are osteocyte-specific; and *MMP13*, *Ctsk*, *Acp5* and *MMP2*, which are all genes known to be involved in PLR.[14, 37-39] It should be noted that the widely used primary osteocyte isolation technique[8, 40, 41] does not exclude the possibility that other bone cells may be present in the population, such as osteoclasts. However, *Dmp1* and *Sost* were highly expressed in all samples, confirming a high purity of osteocytes in the population.[40] *Dmp1* showed a 0.49-fold change in U266 compared to naïve. For the PLR genes, *MMP13* showed a 4.9-fold increase; *Ctsk* a 3.2-fold increase and *Acp5* a 7.7-fold increase compared to naïve. *MMP2*, although not significant, showed a trend for a 1.74-fold increase ($p=0.065$). Despite the upregulation of PLR-specific genes, there was no significant change in *Sost* expression in U266 mice compared to naïve. We did not perform qPCR analysis on the primary osteocytes of 5TGM1 mice owing to their unchanged osteocyte lacunar morphology. To further examine the upregulation of *Acp5* we examined histological sections of U266 bone after staining for

TRAP and found numerous incidences of visible TRAP staining around the nuclei of osteocytes (Supplemental Fig 1Q-R). This helps confirm that the osteocytes are performing osteocytic osteolysis and rules out the possibility that the larger osteocyte lacunae are due to newly formed osteocytes, which typically present with larger lacunae. However, it was impossible to quantify the TRAP staining around the osteocytes, owing to the TRAP staining being too faint as to be confidently identified in many areas.

Increased osteocyte activity is not associated with increased sclerostin production

Since sclerostin is known to stimulate PLR,[14] we next determined whether sclerostin protein levels were increased in U266 bones, though based on the expression data we predicted no significant differences would be seen between disease and naïve bones. Tibial metaphysis sections were stained for sclerostin by IHC (Fig 4D-G) and sclerostin area as a proportion of total bone area was found to be unchanged in disease tibiae (5TGM1 and U266) compared to respective naïves (Fig 4H). Osteocytes were also tagged as to whether they were positive or negative for sclerostin, and the proportion of sclerostin-positive osteocytes was found to be unaltered between disease and naïve tibiae (Fig 4I).

Discussion

Bone disease affects over 90% of myeloma patients, exposing them to chronic pain and high risk of fracture. Current treatments for MBD are limited as they do not repair damaged bones, indicating an unmet clinical need. To improve the treatment of MBD our fundamental knowledge of MBD, particularly the role of osteocytes, needs to improve. Here we set out to understand more about the role of osteocytes and their LCN in MBD by comparing healthy bones to myeloma-bearing bones.

Initially we determined the extent of MBD in two different mouse models and found that both models developed high levels of tumor burden but had differing levels of MBD: mild MBD in 5TGM1 and extensive MBD in U266. SR-μCT showed that osteocyte lacunae proximal to extensive MBD in U266 mice were greatly enlarged and more ellipsoid in comparison to naïve bones. This was not seen in 5TGM1. One reason for the discrepancy between models could be the extent of the osteolytic disease; however, Hemmatian *et al*.[42] reported enlarged osteocyte lacunae in breast and prostate cancer models that both displayed extensive osteolytic disease, but the magnitude of the size change was much smaller than we have found in myeloma. Furthermore, they found the larger lacunae were proximal to osteosclerotic regions rather than osteolytic regions. Another reason could be the timespan of the models used: U266 is a 9-week model, whereas 5TGM1 and the breast and prostate models used by Hemmatian *et al*. are shorter 3-week models, suggesting the osteocyte lacunae require time to become fully enlarged. The discrepancy between the 5TGM1 and U266 model could be further tested by using the JJN3 model, which is a very aggressive 3-week human xenograft model of myeloma that results in very severe MBD. Examining the osteocytes of JJN3 mice would help to confirm whether it is severity of disease or length of disease course that are driving the changes. Finally, it cannot be discounted that 5TGM1 mice have a functional immune system, whereas U266 mice are immunocompromised, and that the presence of an immune system may be why fewer osteocyte and LCN changes are seen in the 5TGM1. This could be tested by examining osteocytes in a more long-course syngeneic model of myeloma such as the 5T2 model;[43] however, access to this mouse model is very limited at present.

We found that substantial MBD decreased osteocyte lacunae density by approximately 20%, in keeping with what has been demonstrated clinically in patients.[15] Vashishth *et al*. have shown that decreased osteocyte density is correlated to an increased accumulation of microcracks, indicating that a dense osteocyte network is linked to better bone quality.[44] We

356 then quantified, for the first time to our knowledge, that MBD leads to an apparent decreased
357 osteocyte canalicular length and overall LCN coverage, and that extensive MBD causes the
358 LCN to be organized differently; similar observational findings were described by Ziouti *et*
359 *al.*[16] The mechanisms behind this apparent canalicular shortening and disorganization are
360 currently unknown, and more work is required to determine how it comes about. It should also
361 be reiterated that the canaliculi were only assessed in 2-D, and that 3-D analysis using a
362 technique such as fluorochromes and confocal microscopy would be beneficial to confirm the
363 shortened canaliculi. However, changes in the LCN such as reduced coverage and shortened
364 canaliculi can affect the mechano-sensing perception of osteocytes, diminishing their ability to
365 initiate appropriate bone remodeling in response to loading or microfracture.[45] These findings
366 may have further reaching clinical implications, as Ding *et al.* demonstrated in their partial
367 osteocyte-ablation murine model that when osteocyte numbers were reduced, rapid
368 development of osteoporosis and signs of early ageing were observed.[46]

369 Osteocytes are known to help maintain bone homeostasis through processes such as sclerostin
370 secretion and PLR. We found no changes either in *Sost* upregulation in osteocytes or localized
371 sclerostin production, concurring with the findings of McDonald *et al*.[19] but contradicting
372 other reported findings. The role of sclerostin in myeloma is clearly complex, and these
373 contrasting conclusions may be due to sclerostin levels fluctuating depending on the severity
374 of MBD and the timepoint at which they are measured in the disease course. It is also true that
375 sclerostin is expressed by other cells within the bone marrow, such as hypertrophic
376 chondrocytes,[47] and that MBD may further influence these expression pathways. However,
377 we did determine that PLR-specific genes were upregulated in osteocyte-enriched populations
378 from bones of extensive MBD-bearing mice. The resorption part-process of PLR (also known
379 as osteocytic osteolysis) involves osteocytes secreting matrix metalloproteinases and enzymes
380 such as cathepsin K and TRAP to dissolve the surrounding bone matrix, and the upregulation

of these related genes provides evidence that PLR is contributing to bone loss in myeloma. To our knowledge, this is the first time that PLR has been proposed as a mechanism of MBD pathophysiology. Interestingly, since sclerostin is known to be a promotor of PLR and its levels in osteocytes were unaffected, other potential drivers of the observed increase in PLR are still to be identified. Aberrant PLR is clearly detrimental to bone health, and this leads to the question of whether PLR-specific genes could be targeted therapeutically in order to normalize osteocyte function. This opens up future avenues of exploration into the cause and consequence of PLR in myeloma.

In summary, we have identified that extensive MBD leads to a decrease in the osteocyte population and an enlargement of osteocyte lacunae. The osteocyte LCN is compromised by MBD, with decreased canalicular length, network area coverage and altered organization. PLR-specific genes are upregulated in the osteocytes in MBD, and further work is needed to explore the ramifications of PLR in myeloma.

Data Availability Statement

The authors confirm that the data supporting the findings of this study are available within the article [and/or] its supplementary materials.

Disclaimers

The authors have no conflicts to report.

Author Contributions

Holly Evans: investigation; methodology; formal analysis; interpretation; writing – original draft; review and editing. **Rebecca Andrews**: conceptualization; funding acquisition; investigation; interpretation; writing – original draft; review and editing. **Fatma Ali Abedi**: investigation; formal analysis; writing – review and editing. **Alexandria Sprules**: investigation;

formal analysis; writing – review and editing. **Jacob Trend**: methodology; investigation; writing – review and editing. **Goran Lovric**: methodology; writing – review and editing. **Alanna Green:** conceptualization; funding acquisition; writing – review and editing. **Andrew Chantry**: funding acquisition; supervision; writing – review and editing. **Janet Brown**: funding acquisition; supervision; writing – review and editing. **Claire Clarkin**: funding acquisition; methodology; writing – review and editing. **Michelle Lawson**: conceptualization; funding acquisition; supervision; interpretation; writing – original draft; review and editing.

Acknowledgements

This work was supported by a Sheffield Hospitals Charity project grant (222323 to RA(PI), HE and ML). Original *in vivo* experiment costs were supported by a Sheffield Hospitals Charity project grant (163969 to RA(PI), AC and ML) and Weston Park Cancer Charity Clinical Research Fellowship (RA (the named clinical fellow), AC, JB). The travel to the SR-μCT facility was funded by a European Association of Cancer Research (EACR) travel award (awarded to RA) and the University of Sheffield travel award (ML). We acknowledge the Paul Scherrer Institut, Villigen, Switzerland for provision of synchrotron radiation beamtime at the TOMCAT beamline X02DA of the SLS (Proposal ID 20220399; HE, RA, AG, ML). The Diamond Light Source is acknowledged for providing beamtime on I13-2 beamline under the experiment number MG31801 (Proposal MG31801; JT), and we thank Dr Shashidhara Marathe for his technical guidance. We also thank Dr Georgia Stewart, Ms Orla Gallagher and Mr Aytac Gul for their technical expertise.

References

[1] Ring ES, Lawson MA, Snowden JA, et al. New agents in the Treatment of Myeloma Bone Disease[J]. *Calcif Tissue Int* 2018,102(2):196-209.
[2] Rosenthal Y, Arami A, Kosashvili Y, et al. Atypical fractures of the femur related to prolonged treatment with bisphosphonates for osteoporosis[J]. *Isr Med Assoc J* 2014,16(2):78-82.

[3] Dallas SL, Prideaux M, Bonewald LF. The osteocyte: an endocrine cell ... and more[J]. *Endocr Rev* 2013,34(5):658-90.
[4] Creecy A, Damrath JG, Wallace JM. Control of Bone Matrix Properties by Osteocytes[J]. *Front Endocrinol (Lausanne)* 2020,11:578477.
[5] Bonewald LF. The amazing osteocyte[J]. *J Bone Miner Res* 2011,26(2):229-38.
[6] Schaffler MB, Cheung WY, Majeska R, et al. Osteocytes: master orchestrators of bone[J]. *Calcif Tissue Int* 2014,94(1):5-24.
[7] Tsourdi E, Jahn K, Rauner M, et al. Physiological and pathological osteocytic osteolysis[J]. *J Musculoskelet Neuronal Interact* 2018,18(3):292-303.
[8] Dole NS, Mazur CM, Acevedo C, et al. Osteocyte-Intrinsic TGF-beta Signaling Regulates Bone Quality through Perilacunar/Canalicular Remodeling[J]. *Cell Rep* 2017,21(9):2585-2596.
[9] Qing H, Ardeshirpour L, Pajevic PD, et al. Demonstration of osteocytic perilacunar/canalicular remodeling in mice during lactation[J]. *J Bone Miner Res* 2012,27(5):1018-29.
[10] Li Y, de Bakker CMJ, Lai X, et al. Maternal bone adaptation to mechanical loading during pregnancy, lactation, and post-weaning recovery[J]. *Bone* 2021,151:116031.
[11] Asagiri M, Takayanagi H. The molecular understanding of osteoclast differentiation[J]. *Bone* 2007,40(2):251-64.
[12] Rolvien T, Krause M, Jeschke A, et al. Vitamin D regulates osteocyte survival and perilacunar remodeling in human and murine bone[J]. *Bone* 2017,103:78-87.
[13] Tokarz D, Martins JS, Petit ET, et al. Hormonal Regulation of Osteocyte Perilacunar and Canalicular Remodeling in the Hyp Mouse Model of X-Linked Hypophosphatemia[J]. *J Bone Miner Res* 2018,33(3):499-509.
[14] Kogawa M, Wijenayaka AR, Ormsby RT, et al. Sclerostin regulates release of bone mineral by osteocytes by induction of carbonic anhydrase 2[J]. *J Bone Miner Res* 2013,28(12):2436-48.
[15] Giuliani N, Ferretti M, Bolzoni M, et al. Increased osteocyte death in multiple myeloma patients: role in myeloma-induced osteoclast formation[J]. *Leukemia* 2012,26(6):1391-401.
[16] Ziouti F, Soares AP, Moreno-Jimenez I, et al. An Early Myeloma Bone Disease Model in Skeletally Mature Mice as a Platform for Biomaterial Characterization of the Extracellular Matrix[J]. *J Oncol* 2020,2020:3985315.
[17] Terpos E, Christoulas D, Katodritou E, et al. Elevated circulating sclerostin correlates with advanced disease features and abnormal bone remodeling in symptomatic myeloma: reduction post-bortezomib monotherapy[J]. *Int J Cancer* 2012,131(6):1466-71.
[18] Delgado-Calle J, Anderson J, Cregor MD, et al. Bidirectional Notch Signaling and Osteocyte-Derived Factors in the Bone Marrow Microenvironment Promote Tumor Cell Proliferation and Bone Destruction in Multiple Myeloma[J]. *Cancer Res* 2016,76(5):1089-100.
[19] McDonald MM, Reagan MR, Youlten SE, et al. Inhibiting the osteocyte-specific protein sclerostin increases bone mass and fracture resistance in multiple myeloma[J]. *Blood* 2017,129(26):3452-3464.
[20] Cosman F, Crittenden DB, Adachi JD, et al. Romosozumab Treatment in Postmenopausal Women with Osteoporosis[J]. *N Engl J Med* 2016,375(16):1532-1543.
[21] Lewiecki EM, Blicharski T, Goemaere S, et al. A Phase III Randomized Placebo-Controlled Trial to Evaluate Efficacy and Safety of Romosozumab in Men With Osteoporosis[J]. *J Clin Endocrinol Metab* 2018,103(9):3183-3193.
[22] Paton-Hough J, Tazzyman S, Evans H, et al. Preventing and Repairing Myeloma Bone Disease by Combining Conventional Antiresorptive Treatment With a Bone Anabolic Agent in Murine Models[J]. *J Bone Miner Res* 2019,34(5):783-796.

[23] Green AC, Lath D, Hudson K, et al. TGFbeta Inhibition Stimulates Collagen Maturation to Enhance Bone Repair and Fracture Resistance in a Murine Myeloma Model[J]. *J Bone Miner Res* 2019,34(12):2311-2326.
[24] Evans HR, Karmakharm T, Lawson MA, et al. Osteolytica: An automated image analysis software package that rapidly measures cancer-induced osteolytic lesions in in vivo models with greater reproducibility compared to other commonly used methods[J]. *Bone* 2016,83:9-16.
[25] Nunez JA, Goring A, Javaheri B, et al. Regional diversity in the murine cortical vascular network is revealed by synchrotron X-ray tomography and is amplified with age[J]. *Eur Cell Mater* 2018,35:281-299.
[26] Nunez JA, Goring A, Hesse E, et al. Simultaneous visualisation of calcified bone microstructure and intracortical vasculature using synchrotron X-ray phase contrast-enhanced tomography[J]. *Sci Rep* 2017,7(1):13289.
[27] Paganin D, Mayo SC, Gureyev TE, et al. Simultaneous phase and amplitude extraction from a single defocused image of a homogeneous object[J]. *J Microsc* 2002,206(Pt 1):33-40.
[28] Lovric G, Oberta P, Mohacsi I, et al. A robust tool for photon source geometry measurements using the fractional Talbot effect[J]. *Opt Express* 2014,22(3):2745-60.
[29] Hemmatian H, Laurent MR, Ghazanfari S, et al. Accuracy and reproducibility of mouse cortical bone microporosity as quantified by desktop microcomputed tomography[J]. *PLoS One* 2017,12(8):e0182996.
[30] Lawson MA, Paton-Hough JM, Evans HR, et al. NOD/SCID-GAMMA mice are an ideal strain to assess the efficacy of therapeutic agents used in the treatment of myeloma bone disease[J]. *PLoS One* 2015,10(3):e0119546.
[31] Lath DL, Buckle CH, Evans HR, et al. ARQ-197, a small-molecule inhibitor of c-Met, reduces tumour burden and prevents myeloma-induced bone disease in vivo[J]. *PLoS One* 2018,13(6):e0199517.
[32] Ploton D, Menager M, Jeannesson P, et al. Improvement in the staining and in the visualization of the argyrophilic proteins of the nucleolar organizer region at the optical level[J]. *Histochem J* 1986,18(1):5-14.
[33] Schindelin J, Arganda-Carreras I, Frise E, et al. Fiji: an open-source platform for biological-image analysis[J]. *Nat Methods* 2012,9(7):676-82.
[34] Ikpegbu E, Basta L, Clements DN, et al. FGF-2 promotes osteocyte differentiation through increased E11/podoplanin expression[J]. *J Cell Physiol* 2018,233(7):5334-5347.
[35] Bankhead P, Loughrey MB, Fernandez JA, et al. QuPath: Open source software for digital pathology image analysis[J]. *Sci Rep* 2017,7(1):16878.
[36] Livak KJ, Schmittgen TD. Analysis of relative gene expression data using real-time quantitative PCR and the 2(-Delta Delta C(T)) Method[J]. *Methods* 2001,25(4):402-8.
[37] Mazur CM, Woo JJ, Yee CS, et al. Osteocyte dysfunction promotes osteoarthritis through MMP13-dependent suppression of subchondral bone homeostasis[J]. *Bone Res* 2019,7:34.
[38] Fowler TW, Acevedo C, Mazur CM, et al. Glucocorticoid suppression of osteocyte perilacunar remodeling is associated with subchondral bone degeneration in osteonecrosis[J]. *Sci Rep* 2017,7:44618.
[39] Inoue K, Mikuni-Takagaki Y, Oikawa K, et al. A crucial role for matrix metalloproteinase 2 in osteocytic canalicular formation and bone metabolism[J]. *J Biol Chem* 2006,281(44):33814-24.
[40] Youlten SE, Kemp JP, Logan JG, et al. Osteocyte transcriptome mapping identifies a molecular landscape controlling skeletal homeostasis and susceptibility to skeletal disease[J]. *Nat Commun* 2021,12(1):2444.

[41] Dole NS, Yee CS, Schurman CA, et al. Assessment of Osteocytes: Techniques for Studying Morphological and Molecular Changes Associated with Perilacunar/Canalicular Remodeling of the Bone Matrix[J]. *Methods Mol Biol* 2021,2230:303-323.
[42] Hemmatian H, Conrad S, Furesi G, et al. Reorganization of the osteocyte lacuno-canalicular network characteristics in tumor sites of an immunocompetent murine model of osteotropic cancers[J]. *Bone* 2021,152:116074.
[43] Croese JW, Vas Nunes CM, Radl J, et al. The 5T2 mouse multiple myeloma model: characterization of 5T2 cells within the bone marrow[J]. *Br J Cancer* 1987,56(5):555-60.
[44] Vashishth D, Verborgt O, Divine G, et al. Decline in osteocyte lacunar density in human cortical bone is associated with accumulation of microcracks with age[J]. *Bone* 2000,26(4):375-80.
[45] Price C, Zhou X, Li W, et al. Real-time measurement of solute transport within the lacunar-canalicular system of mechanically loaded bone: direct evidence for load-induced fluid flow[J]. *J Bone Miner Res* 2011,26(2):277-85.
[46] Ding P, Gao C, Gao Y, et al. Osteocytes regulate senescence of bone and bone marrow[J]. *Elife* 2022,11.
[47] Winkler DG, Sutherland MK, Geoghegan JC, et al. Osteocyte control of bone formation via sclerostin, a novel BMP antagonist[J]. *EMBO J* 2003,22(23):6267-76.

Figure legends

Figure 1. Extent of myeloma bone disease in 5TGM1 and U266 murine models. Study schematics of (A) 5TGM1 and (B) U266 models, BKAL and NSG mice were used as naïve control groups respectively. Representative images of tibial hematoxylin-stained sections of bone marrow from (C) naïve (BKAL) and (D) 5TGM1, and (E) naïve (NSG) and (F) U266. Tibial TRAP-stained sections show endocortical bone surface of (G) naïve (BKAL) and (H) 5TGM1, and (I) naïve (NSG) and (J) U266, showing distribution of osteoblasts (red arrows) and osteoclasts (blue arrows). Histomorphometric analysis of (K) tumor burden, (L) osteoblast surface and (M) osteoclast surface. Representative images of bone lesions and trabecular structure found in the distal femur of (N) naïve (BKAL) and (O) 5TGM1, and (P) naïve (NSG) and (Q) U266; tibiofibular joint region of (R) naïve (BKAL) and (S) 5TGM1; and μCT analysis at the distal femur assessing (T) osteolytic lesion area, (U) cortical bone volume, (V) cortical thickness and (W) trabecular bone volume. BM=bone marrow, T=tumor, EC=endocortical.

562 Data are presented as mean ±SD. *p<0.05, **p<0.01, ***p<0.001, ****p<0.0001 (unpaired
563 two-tailed Student's t-test).

564

565 **Figure 2. Osteocyte lacunae density is less in U266 mice with larger and more ellipsoidal**
566 **lacunae.** SR-μCT analysis of the osteocyte lacunae in 5TGM1, U266 or respective naive mice
567 at the femoral metaphysis showing (A) osteocyte lacunae density, (B) osteocyte lacunae as a
568 proportion of the bone, (C) average osteocyte lacunar volume, and (D) average osteocyte
569 lacunar sphericity. Representative images of (E) naïve (BKAL), (F) 5TGM1, (G) naïve (NSG)
570 and (H) U266 femoral metaphysis regions assessed by SR-μCT with individual osteocyte
571 lacunae false color-mapped by volume. Representative SR-μCT images of (I) naïve (NSG) and
572 (J) U266 mice femoral cortical bone showing typical osteocyte lacunae. Phase-contrast
573 imaging of the same U226 bone using false-color mapping and (L) zoomed-in imaging showing
574 dark blue osteocytes sitting within the enlarged osteocyte lacunae (white arrows). BV=blood
575 vessel, OL=osteolytic lesion. All data shown as mean ±SD. **p<0.01, ***p<0.001,
576 ****p<0.0001 (unpaired two-tailed Student's t-test).

577

578 **Figure 3. Myeloma bone disease leads to apparent shortening of osteocyte canalicular**
579 **length and decreased LCN area coverage.** Analysis of the LCN showing (A) canalicular
580 length and (B) LCN area coverage. Representative Ploton silver nitrate-stained images of tibial
581 cortical bone of (C) naïve (BKAL), (D) 5TGM1, (E) naïve (NSG) and (F) U266, showing
582 osteocytes and the LCN. Analysis of LCN organization by (G) aligning osteocytes
583 perpendicular to bone lamellae (0°) and assessing degrees of alignment of canaliculi to 0°, and
584 (H) proportion of canaliculi aligned within 40° of 0°. Representative images of canalicular
585 orientation of (I) naïve (BKAL), (J) 5TGM1, (K) naïve (NSG) and (L) U266, with aligned

canaliculi in blue and unaligned canaliculi in red. All data shown as mean ±SD. * $p<0.05$, **$p<0.01$, ****$p<0.0001$ (unpaired two-tailed Student's t-test).

Figure 4. Myeloma bone disease leads to up-regulation of PLR-specific genes but not *Sost*. Representative bioluminescent imaging of U266 tumor burden (A) and *in vivo* μCT of the distal femur (B) showing bone lesions. (C) qPCR analysis of osteocyte-specific genes *Dmp1* and *Sost*, and PLR genes *MMP13*, *Ctsk*, *Acp5* and *MMP2* relative to *Gapdh* expression. Representative images of sclerostin staining of tibial cortical bone of (D) naïve (BKAL), (E) 5TGM1, (F) naïve (NSG) and (G) U266, with red arrows indicating sclerostin-positive osteocytes and white arrows indicating sclerostin-negative osteocytes. Analysis of sclerostin IHC showing (H) proportional sclerostin staining coverage and (I) proportion of sclerostin-positive osteocytes. All data shown as mean ±SD. *$p<0.05$ (unpaired two-tailed Student's t-test).

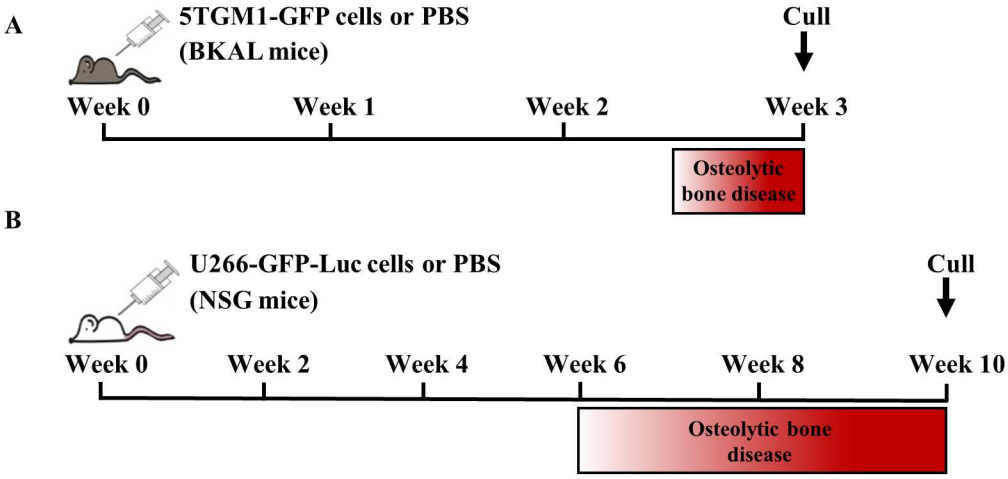
A
5TGM1-GFP cells or PBS
(BKAL mice)
Cull
Week 0
Week 1
Week 2
Week 3
Osteolytic
bone disease
B
U266-GFP-Luc cells or PBS
(NSG mice)
Cull
Week 0
Week 2
Week 4
Week 6
Week 8
Week 10
Osteolytic bone
disease

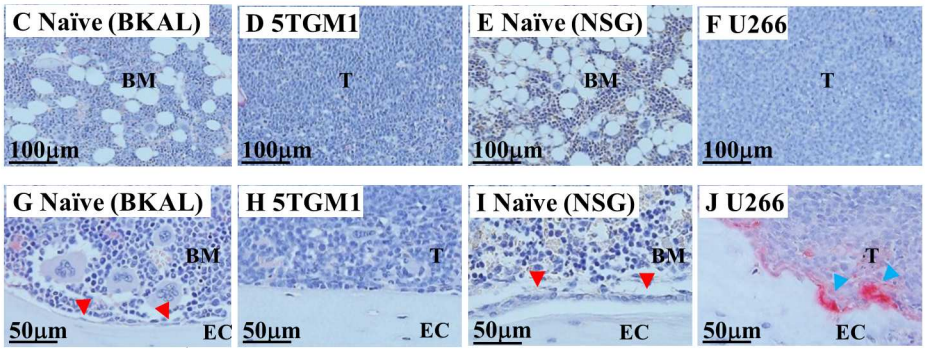
C Naïve (BKAL)
BM
100µm
D 5TGM1
T
100µm
E Naïve (NSG)
BM
100µm
F U266
T
100µm
G Naïve (BKAL)
BM
50µm
EC
H 5TGM1
T
50µm
EC
I Naïve (NSG)
BM
50µm
EC
J U266
T
50µm
EC

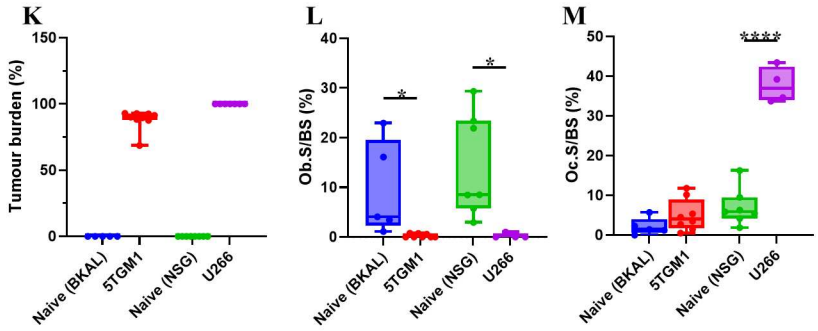
K
Tumour burden (%)
150
100
50
0
Naïve (BKAL)
5TGM1
Naïve (NSG)
U266
L
Ob.S/BS (%)
40
30
20
10
0
*
*
Naïve (BKAL)
5TGM1
Naïve (NSG)
U266
M
Oc.S/BS (%)
50
40
30
20
10
0
****
Naïve (BKAL)
5TGM1
Naïve (NSG)
U266

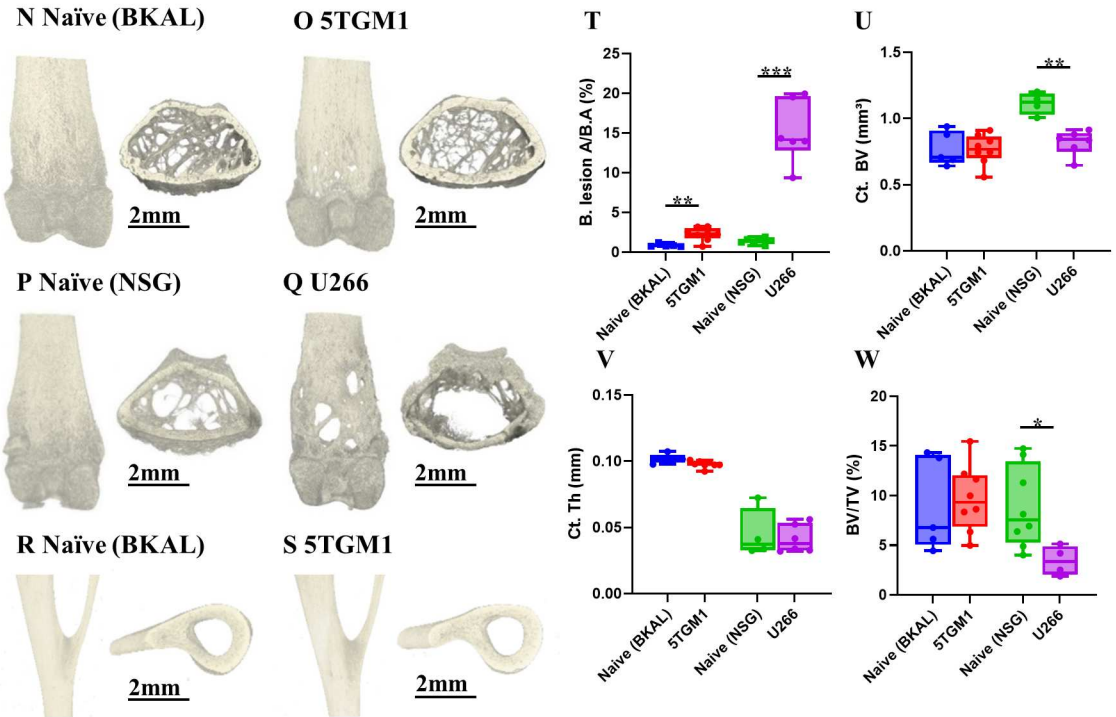
N Naïve (BKAL)
O 5TGM1
2mm
2mm
P Naïve (NSG)
Q U266
2mm
2mm
R Naïve (BKAL)
S 5TGM1
2mm
2mm
T
B. lesion A/B.A (%)
25
20
15
10
5
0
**
***
Naïve (BKAL)
5TGM1
Naïve (NSG)
U266
U
Ct. BV (mm³)
1.5
1.0
0.5
0.0
**
Naïve (BKAL)
5TGM1
Naïve (NSG)
U266
V
Ct. Th (mm)
0.15
0.10
0.05
0.00
Naïve (BKAL)
5TGM1
Naïve (NSG)
U266
W
BV/TV (%)
20
15
10
5
0
*
Naïve (BKAL)
5TGM1
Naïve (NSG)
U266

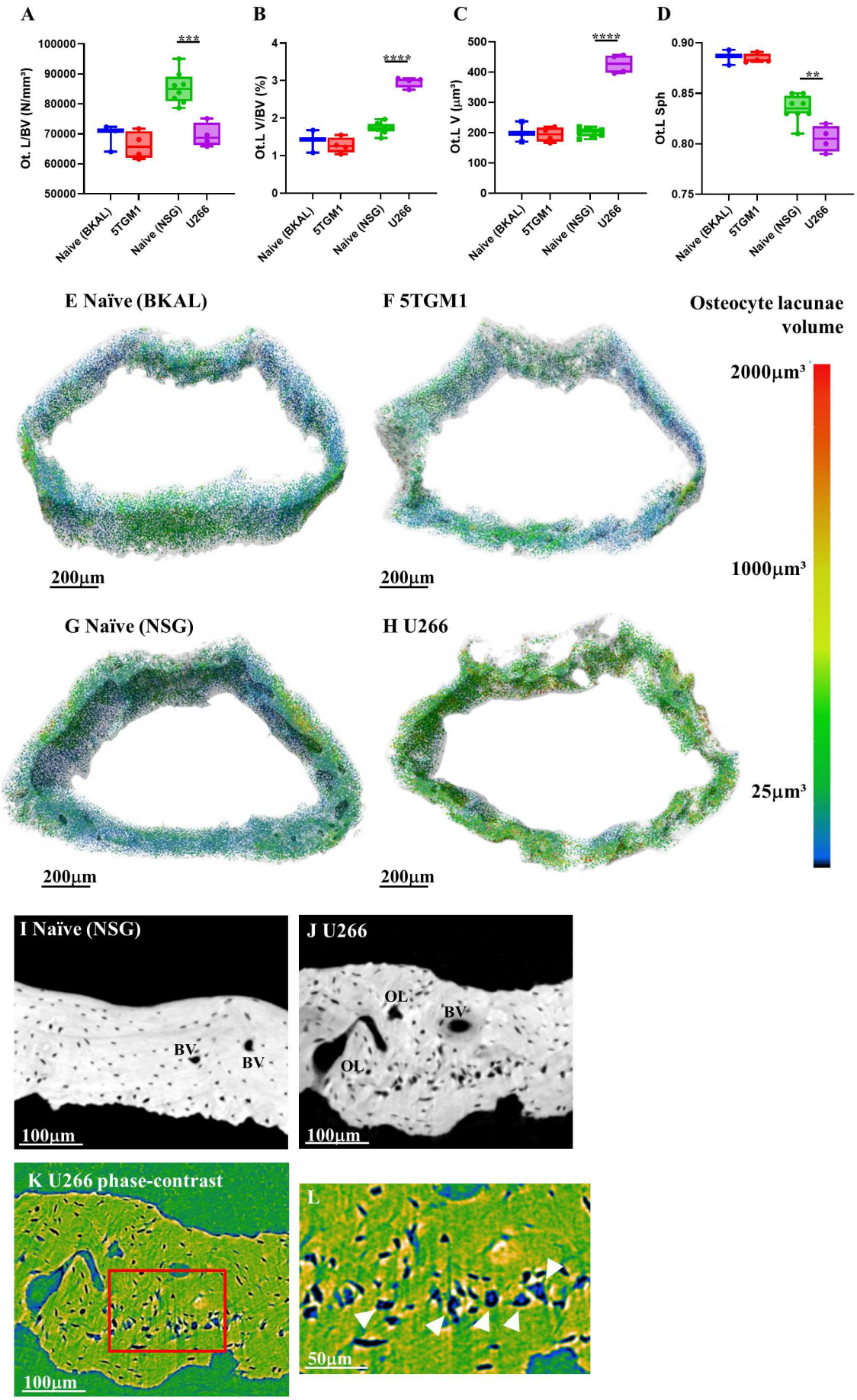
A
B
C
D
Ot. L/BV (N/mm³)
Ot.L V/BV (%)
Ot.L V (µm³)
Ot.L Sph
***
****
****
**
Naive (BKAL)
5TGM1
Naive (NSG)
U266
E Naïve (BKAL)
F 5TGM1
Osteocyte lacunae volume
2000µm³
1000µm³
25µm³
200µm
G Naïve (NSG)
H U266
I Naïve (NSG)
J U266
BV
OL
100µm
K U266 phase-contrast
L
50µm

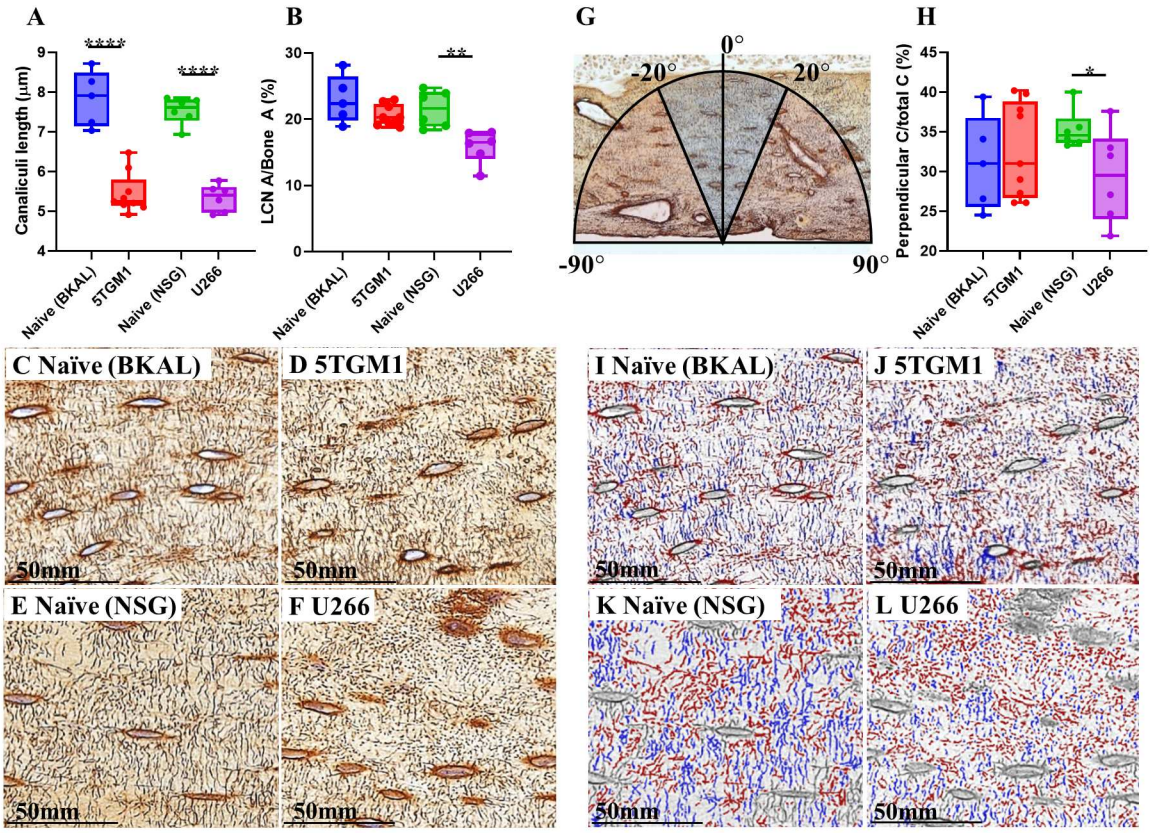
A
B
G
H
Canaliculi length (μm)
LCN A/Bone A (%)
Perpendicular C/total C (%)
****
****
**
*
0°
-20°
20°
-90°
90°
Naïve (BKAL)
5TGM1
Naive (NSG)
U266
C Naïve (BKAL)
D 5TGM1
E Naïve (NSG)
F U266
I Naïve (BKAL)
J 5TGM1
K Naïve (NSG)
L U266
50mm

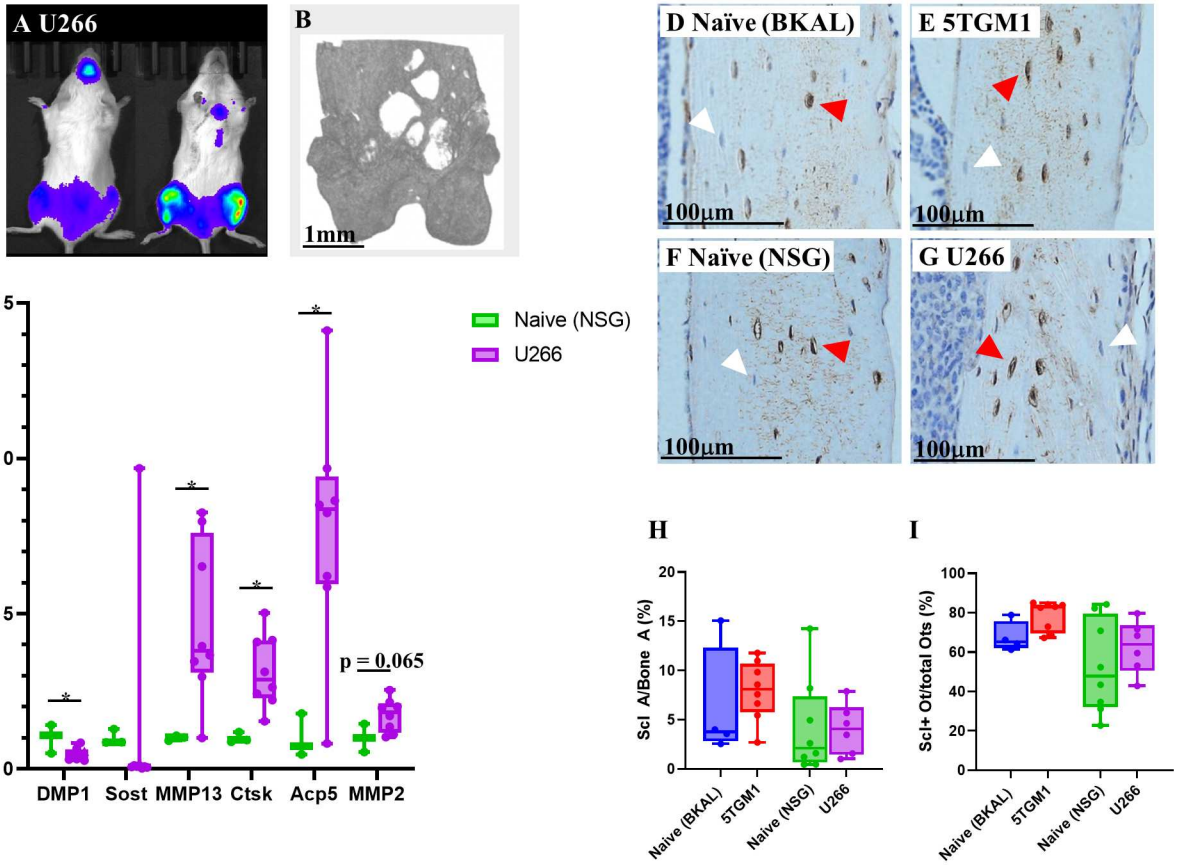
A U266
B
1mm
C
Fold mRNA levels
15
10
5
0
DMP1
Sost
MMP13
Ctsk
Acp5
MMP2
p = 0.065
Naive (NSG)
U266
D Naïve (BKAL)
E 5TGM1
F Naïve (NSG)
G U266
100µm
H
Scl A/Bone A (%)
20
15
10
5
0
Naive (BKAL)
5TGM1
Naive (NSG)
U266
I
Scl+ Ot/total Ots (%)
100
80
60
40
20
0
Naive (BKAL)
5TGM1
Naive (NSG)
U266

Supplementary figure legends

Supplementary Figure 1. Osteocytes are unchanged at the TFJ in 5TGM1 mice. Histomorphometric analysis of (A) osteoblast number and (B) osteoclast number. μCT analysis at the distal femur assessing (C) trabecular thickness, (D) trabecular number and (E) trabecular separation. Representative images of (F) the femoral metaphysis region scanned highlighted by the black box and the resulting 500μm region imaged and analyzed at 0.65μm resolution and (G) the tibiofibular joint region scanned highlighted by the black box and the resulting 500μm region imaged and analyzed at 0.65μm resolution. (H) Image of a femur to be scanned, mounted on a metal chuck and glued in place. Representative image of (I) the femoral metaphysis showing successfully isolated osteocyte lacunae in yellow and (J) a zoomed-in region showing the successful exclusion of blood vessels (white arrows). SR-μCT analysis of the osteocyte lacunae in 5TGM1 at the tibiofibular joint showing (K) osteocyte lacunae density, (L) osteocyte lacunae volume as proportion of the bone, (M) average osteocyte lacunar volume and (N) average osteocyte lacunar sphericity. Representative images of (O) naïve (BKAL) and (P) 5TGM1 tibiofibular joint regions with the individual osteocyte lacunae false color-mapped by volume. Representative images of tibial TRAP-stained sections of endocortical bone of (Q) naïve (NSG) and (R) U266, 1.5mm from the growth plate, showing osteocytes (red arrows) and TRAP staining (pink). Osteoclasts are also highlighted (blue arrows). BM=bone marrow, EC=endocortical. All data shown as mean ±SD. *<0.05, ***p<0.001 (unpaired two-tailed Student's t-test).

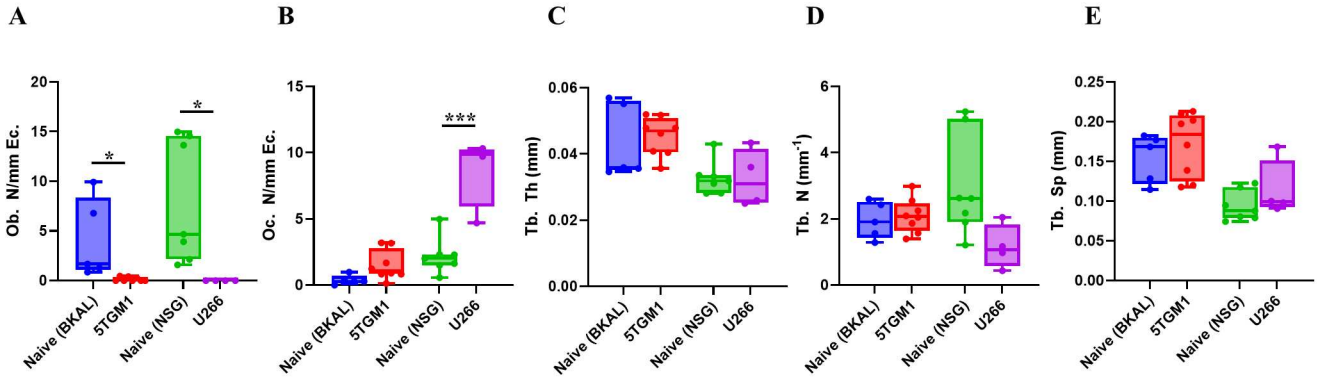
A
B
C
D
E
Ob. N/mm Ec.
Oc. N/mm Ec.
Tb. Th (mm)
Tb. N (mm⁻¹)
Tb. Sp (mm)
Naive (BKAL)
5TGM1
Naive (NSG)
U266
*
*
***

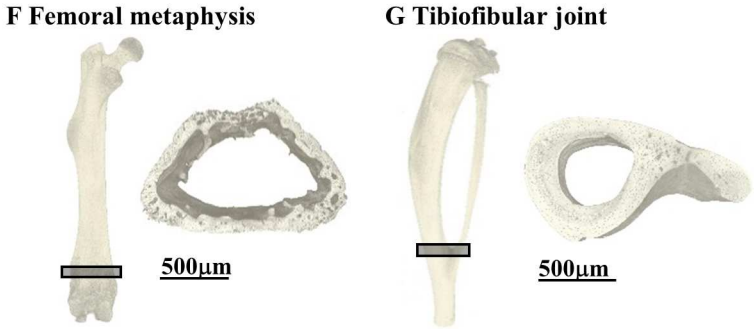
F Femoral metaphysis
G Tibiofibular joint
500µm
500µm

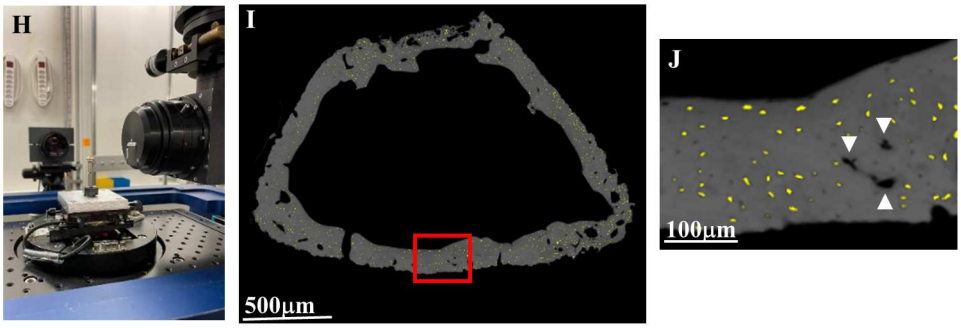
H
I
J
500µm
100µm

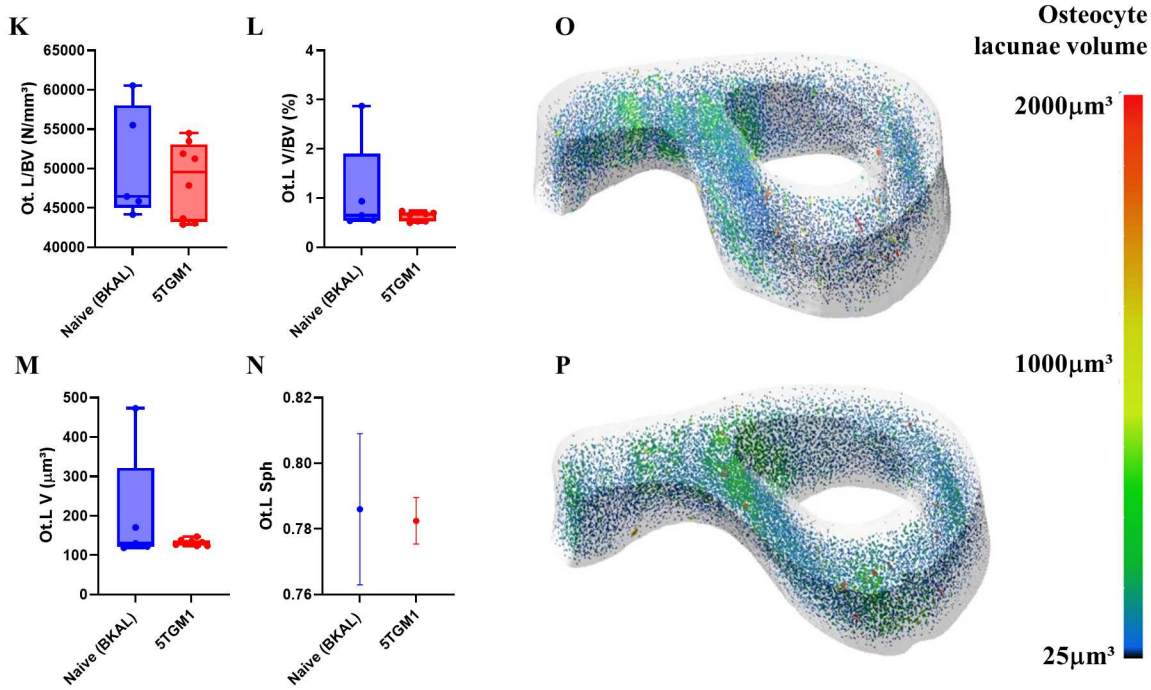
K
L
O
M
N
P
Osteocyte lacunae volume
2000µm³
1000µm³
25µm³
Ot. L/BV (N/mm³)
Ot.L V/BV (%)
Ot.L V (µm³)
Ot.L Sph
Naive (BKAL)
5TGM1

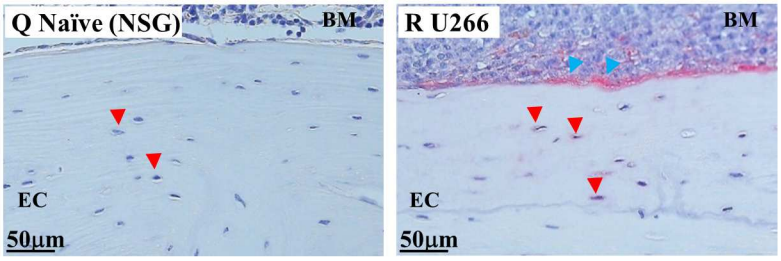
Q Naïve (NSG)
R U266
BM
EC
50µm